Eliminating Interface Reflections in Hybrid Low-Dispersion FDTD Algorithms

Mohammed F. Hadi[1] **and Rabie K. Dib**[2]

[1]Electrical Engineering Dept., Kuwait University, P. O. Box 5969, Safat 13060, Kuwait
[2]College of Technological Studies, PAAET, P. O. Box 4196, Hawalli 32072, Kuwait

Abstract— The numerical phase mismatch across FDTD lattice layers with different sets of update equations has been investigated. A predictive equation of numerical reflections across high-order/low-order layers has been derived. Based on this equation the standard Yee (S_{22}) update equations have been modified to allow their implementation around PEC boundaries and other special situations in an otherwise global high-order implementation, while keeping spurious reflections at the hybrid interface to a practical minimum and independent of the traversing wave direction. S_{22} Phase matching has been developed and verified in both S_{24} and M24 high-order hybrid algorithms.

Keywords— FDTD, Numerical Dispersion, High-Order Schemes, Phase-Matching, Electrically Large Structures.

I. INTRODUCTION

SEVERAL FDTD algorithms have been developed over the past decade to minimize the loss of phase coherency in wave solutions due to numerical dispersion. Shlager and Schneider [1] compared some of the more prominent low-dispersion algorithms and compared their phase coherency for both single-frequency and wideband use. While some of the analyzed algorithms that restricted their stencils to a single Yee cell did extremely well for single-frequency use [2] and [3], it was the two-dimensional extended-stencil M24 algorithm [4] that excelled in both single-frequency and wideband suitability. The M24 algorithm utilizes multiple weighted Ampere's and Faraday's loop integrals over extended FDTD stencils as demonstrated in Fig. 1. In comparison, the S_{24} algorithm (second-order in time and fourth-order in space finite differences) which will also be discussed in this present work is a special case of the M24 algorithm when the outermost loop integral in Fig. 1 is omitted and K_1 is set to $-1/8$.

The main challenge to such extended-stencil algorithms, however, is porting the wealth of FDTD tools that were developed over the decades for the standard single-cell Yee algorithm (S_{22} for second-order differencing in both time and space). It was suggested in [4] that this challenge could be simply resolved by introducing minimal S_{22} buffer zones where needed in an otherwise global M24 implementation. Haussmann in [5], however, demonstrated experimentally that such an approach would cause measurable reflections at the interface between the high-order and low-order zones. Another approach pursued by Georgakopoulos *et al.* in [6] was using a fine-meshed S_{22} buffer zone that would better match its dispersion characteristics to a coarsely-meshed S_{24} zone. Both works, however, left open the questions as to the extent of interface reflections at oblique wave incidence angles as well as to the optimum mesh size ratio between the high-order and low-order zones.

Recently, Celuch-Marcysiak and Rudnicki [7] and [8] developed a methodology for predicting numerical reflections at normal and oblique angles of incidence across dissimilarly gridded homogeneous zones and went on to validate them using FDTD simulations. In this present work this same methodology will be applied to derive appropriate equations to predict the reflection coefficient across similarly gridded homogeneous zones but with varying differencing schemes (in particular, S_{24}/S_{22} and M24/S_{22} interfaces) and quantify the limitations of using S_{22} buffer zones within high-order FDTD implementations. As in [8], the effect of nonorthogonality of wave polarization to propagation direction (wavenumber vector) [9] will be accounted for. Furthermore, new update equations for the S_{22} buffer zone will be developed and validated that will utilize single-cell depth normal to the interface plane and extended-cell depth tangentially to eliminate cross-interface reflections while still being usable near PEC boundaries and other special situations. In effect, realizing optimum phase matching (minimal interface reflections) without the need for S_{22} subgridding.

II. FDTD RENDITION OF PLANE WAVES

When an FDTD algorithm attempts to propagate a plane wave it introduces two types of numerical dispersion-related errors that are of interest to us here. The first is the error in the rendered numerical

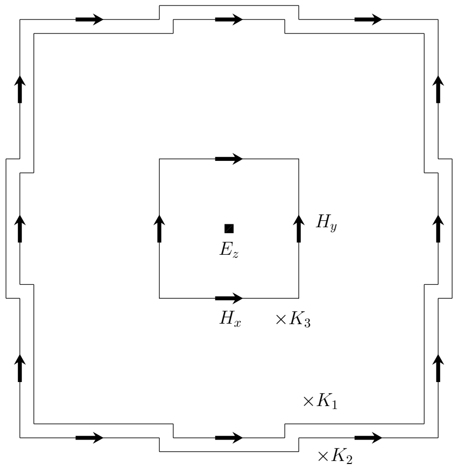

Fig. 1. Multiple weighted Ampere's loops for updating a centered E_z node in the M24 algorithm. A uniform $\Delta x = \Delta y = h$ is assumed and $K_3 = 1 - K_1 - K_2$.

wavenumber that causes the accumulation of phase error as the wave traverses the numerical domain. This error is a function of the propagation angle and resolution factor (number of FDTD cells per wavelength, R) and is well documented in the literature. The other type of error is the one that affects the polarization of the propagating wave. It was demonstrated in [9] and [10] that as the wave bounces around in the FDTD lattice the orthogonal $\bar{E}$ and $\bar{H}$ vectors form a numerical Poynting vector that is not parallel to the propagation direction

$$\bar{\beta} = \bar{a}_x\beta_x + \bar{a}_y\beta_y + \bar{a}_z\beta_z \tag{1}$$

but rather to

$$\bar{P} = \bar{a}_x D_x + \bar{a}_y D_y + \bar{a}_z D_z, \tag{2}$$

where D_x, D_y and D_z are discrete operators dictated by the FDTD algorithm of interest, and β_x, β_y and β_z are the numerically rendered wavenumber components that can be derived from the algorithm's dispersion relation.

A. Discrete Operators

The standard S_{22} algorithm in 2–D implementations has the discrete operators

$$D_x = \frac{\sin\frac{\beta_x h}{2}}{h/2} \quad \text{and} \quad D_y = \frac{\sin\frac{\beta_y h}{2}}{h/2}. \tag{3}$$

The M24 algorithm, on the other hand, has the update equations [4] (see Fig. 1)

$$\begin{aligned}
\epsilon\frac{\partial E_z}{\partial t} \;=\;& \frac{K_1}{3h}\begin{pmatrix} H_x|_{j-\frac{3}{2}} - H_x|_{j+\frac{3}{2}} \\ +H_y|_{i+\frac{3}{2}} - H_y|_{i-\frac{3}{2}} \end{pmatrix} \\
&+\frac{K_2}{6h}\begin{pmatrix} H_x|_{i-1,j-\frac{3}{2}} + H_x|_{i+1,j-\frac{3}{2}} \\ -H_x|_{i-1,j+\frac{3}{2}} - H_x|_{i+1,j+\frac{3}{2}} \\ +H_y|_{i+\frac{3}{2},j-1} + H_y|_{i+\frac{3}{2},j+1} \\ -H_y|_{i-\frac{3}{2},j-1} - H_y|_{i-\frac{3}{2},j+1} \end{pmatrix} \\
&+\frac{K_3}{h}\begin{pmatrix} H_x|_{j-\frac{1}{2}} - H_x|_{j+\frac{1}{2}} \\ +H_y|_{i+\frac{1}{2}} - H_y|_{i-\frac{1}{2}} \end{pmatrix},
\end{aligned} \tag{4}$$

$$\begin{aligned}
\mu\frac{\partial H_x}{\partial t} \;=\;& \frac{K_1}{3h}\left(E_z|_{j-\frac{3}{2}} - E_z|_{j+\frac{3}{2}}\right) \\
&+\frac{1-K_1}{h}\left(E_z|_{j-\frac{1}{2}} - E_z|_{j+\frac{1}{2}}\right),
\end{aligned} \tag{5}$$

$$\begin{aligned}
\mu\frac{\partial H_y}{\partial t} \;=\;& \frac{K_1}{3h}\left(E_z|_{i+\frac{3}{2}} - E_z|_{i-\frac{3}{2}}\right) \\
&+\frac{1-K_1}{h}\left(E_z|_{i+\frac{1}{2}} - E_z|_{i-\frac{1}{2}}\right)
\end{aligned} \tag{6}$$

where non-staggered indices are omitted for cleaner notation and $K_3 = 1 - K_1 - K_2$. These K parameters are chosen through an optimization routine that will ensure minimal dispersion error across all angles of propagation in the numerical lattice. The corresponding discrete operators are given by

$$\begin{aligned}
D_x^y \;=\;& K_3\frac{\sin\frac{\beta_x h}{2}}{h/2} \\
&+\left(K_1 + K_2\cos\beta_y h\right)\frac{\sin\frac{3\beta_x h}{2}}{3h/2},
\end{aligned} \tag{7}$$

$$D_x^z = (1-K_1)\frac{\sin\frac{\beta_x h}{2}}{h/2} + K_1\frac{\sin\frac{3\beta_x h}{2}}{3h/2}, \tag{8}$$

$$\begin{aligned}
D_y^x \;=\;& K_3\frac{\sin\frac{\beta_y h}{2}}{h/2} \\
&+\left(K_1 + K_2\cos\beta_x h\right)\frac{\sin\frac{3\beta_y h}{2}}{3h/2},
\end{aligned} \tag{9}$$

$$D_y^z = (1-K_1)\frac{\sin\frac{\beta_y h}{2}}{h/2} + K_1\frac{\sin\frac{3\beta_y h}{2}}{3h/2}. \tag{10}$$

The operator notation for the M24 algorithm is slightly different than that of the S_{22}'s as an x, y or z superscript on the discrete operator denotes its restricted applicability to that particular field component. On the other hand, the S_{22} operators are linear; $D_x^y = D_x^z = D_x$ and $D_y^x = D_y^z = D_y$.

When K_1 and K_2 are substituted with $-1/8$ and zero, respectively, equations (4) to (10) produce the corresponding update equations and discrete operators for the S_{24} algorithm. In particular, the latter will be linear;

$$D_x = \frac{9}{8}\frac{\sin\frac{\beta_x h}{2}}{h/2} - \frac{1}{8}\frac{\sin\frac{3\beta_x h}{2}}{3h/2}, \tag{11}$$

$$D_y = \frac{9}{8}\frac{\sin\frac{\beta_y h}{2}}{h/2} - \frac{1}{8}\frac{\sin\frac{3\beta_y h}{2}}{3h/2}. \tag{12}$$

B. Dispersion Relations

The generalized dispersion relation for FDTD algorithms can be conveniently written in the form [5]

$$\mu\epsilon D_t^2 = D_x^y D_x^z + D_y^x D_y^z + D_z^x D_z^y \tag{13}$$

with

$$D_t = -\frac{\sin\frac{\omega\Delta t}{2}}{\Delta t/2}, \tag{14}$$

provided that

$$D_y^z D_z^x D_x^y = D_z^y D_x^z D_y^x. \tag{15}$$

This latter condition is not a problem for 2-D algorithms with nonlinear operators as is the case with the M24 algorithm since $D_z^x = D_z^y = 0$. For linear-operator algorithms (S_{22} and S_{24}), equation (13) can be reduced to

$$\mu\epsilon D_t^2 = D_x^2 + D_y^2 + D_z^2. \tag{16}$$

Direct substitutions of equations (3) and (11) to (12) into (16), and equations (7) to (10) into (13) will produce the dispersion relations for the S_{22}, S_{24} and M24 algorithms.

C. Stability Criteria

The maximum allowable time step before the onset of numerical instability for FDTD algorithms with linear discrete operators and second-order differencing in time is given by,

$$\Delta t \le \frac{2\sqrt{\mu\epsilon}}{\sqrt{(D_x^2 + D_y^2 + D_z^2)_{\max}}} \tag{17}$$

while for 2-D such algorithms with nonlinear operators it is given by,

$$\Delta t \le \frac{2\sqrt{\mu\epsilon}}{\sqrt{\left(D_x^y D_x^z + D_y^x D_y^z\right)_{\max}}} \tag{18}$$

where the "max" condition exists at $\beta_x h = \beta_y h = \pi$ or its odd multiples. These two inequalities will provide the well known S_{22} and S_{24} stability criteria,

$$\Delta t_{S22} \le \frac{h}{c\sqrt{2}} \quad \text{and} \quad \Delta t_{S24} \le \frac{(6/7)h}{c\sqrt{2}} \tag{19}$$

as well as

$$\Delta t_{M24} \le \frac{h}{c\sqrt{2}} \frac{3}{\sqrt{(3-4K_1)(3-4K_1-2K_2)}}. \tag{20}$$

In hybrid S_{24}/S_{22} or M24/S_{22} implementations the corresponding S_{24} or M24 time steps need to be used to avoid instability since they would be slightly smaller than the S_{22}'s maximum time step. Finally, it should be mentioned here that $\sqrt{-1}$ factors have been omitted from all the discrete operators since they would eventually cancel out for our purposes here.

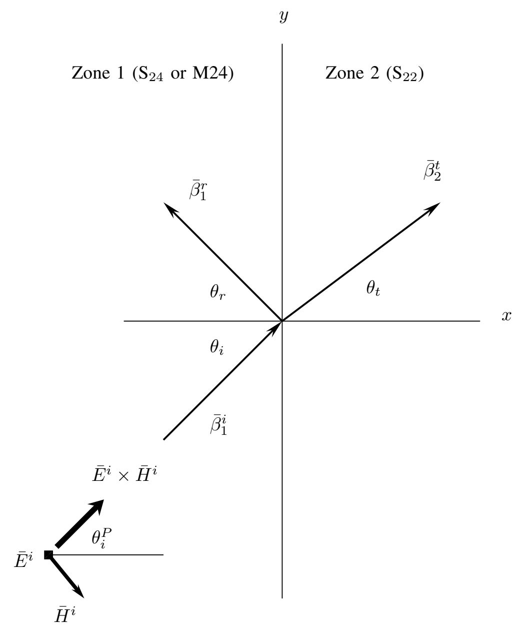

Fig. 2. Interpretation of a plane wave interaction with a planar interface separating two similarly gridded homogeneous zones with different FDTD schemes. Field nodes on the y-axis are assumed part of zone 2.

III. NUMERICAL REFLECTION COEFFICIENT

Let us assume a planar interface in a standard FDTD lattice is being traversed at an oblique angle of incidence from left to right with the medium at both sides of the interface being free space (see Fig. 2). Let us also assume that S_{22} update equations are used in the right zone including field nodes coinciding with the planar interface itself. In the left zone we will be using the update equations of the algorithm under study (S_{24} or M24). In either zone of this FDTD lattice the relationship between the direction of propagation and wavenumber is governed by,

$$\bar{\beta} = \bar{a}_x\beta_x + \bar{a}_y\beta_y = \bar{a}_x\beta\cos\theta + \bar{a}_y\beta\sin\theta \tag{21}$$

where θ could be θ_i, θ_r or θ_t (incidence, reflection or transmission angles) and β could be β_1 or β_2, the numerical wavenumbers which are the solutions of the dispersion relations corresponding to either zonal algorithm. From equation (2) we can write

$$\bar{P} = \bar{a}_x P\cos\theta^P + \bar{a}_y P\sin\theta^P \tag{22}$$

where, again, θ^P could be θ_i^P, θ_r^P or θ_t^P and is calculated from

$$\theta^P = \tan^{-1}\frac{D_y}{D_x}. \tag{23}$$

A $\theta = \theta^P = 0$ means both propagation and Poynting vectors are normal to the interface. Since we are using uniform space meshing in both zones we can assume that $\theta_r = \theta_i$ and $\theta_r^P = \theta_i^P$, with the latter being due to numerical dispersion symmetry around $\theta = 0$. Also, at the planar interface ($x = 0$), boundary conditions will force

$$\beta_{1y} = \beta_{2y} \tag{24}$$

since both zonal algorithms share the same field nodes at the interface and the incident, transmitted and possibly reflected field amplitudes are related by $E_{1o}^i + E_{1o}^r = E_{2o}^t$. We will also be using $E_{1o}^r = \Gamma E_{1o}^i$ where Γ is the desired numerical reflection coefficient.

The S_{22} update equation for the E_z field node at the interface (say, at the $x = 0$ and $y = 0$ location) is

$$E_z|_{0,0}^{n+\frac{1}{2}} - E_z|_{0,0}^{n-\frac{1}{2}} = \frac{\Delta t}{\epsilon h}\left(\begin{array}{c} H_y|_{\frac{1}{2},0}^{n} - H_y|_{-\frac{1}{2},0}^{n} \\ -H_x|_{0,\frac{1}{2}}^{n} + H_x|_{0,-\frac{1}{2}}^{n}\end{array}\right). \tag{25}$$

Assuming that each of the above field nodes has the form $e^{j(\omega t - \beta_x x - \beta_y y)}$ we can replace them, each (after eliminating common terms) with

$$E_z|_{0,0}^{n\pm\frac{1}{2}} \rightarrow (1+\Gamma)E_{1o}^i e^{\pm j\omega\Delta t/2}, \tag{26}$$

$$H_y|_{\frac{1}{2},0}^{n} \rightarrow -\frac{(1+\Gamma)E_{1o}^i}{\eta}\cos\theta_t^P e^{-j\beta_{2x}h/2}, \tag{27}$$

$$H_y|_{-\frac{1}{2},0}^{n} \rightarrow -\frac{E_{1o}^i}{\eta}\cos\theta_i^P e^{j\beta_{1x}h/2} + \frac{\Gamma E_{1o}^i}{\eta}\cos\theta_i^P e^{-j\beta_{1x}h/2}, \tag{28}$$

$$H_x|_{0,\frac{1}{2}}^{n} \rightarrow \frac{E_{1o}^i}{\eta}\sin\theta_i^P e^{-j\beta_{1y}h/2} + \frac{\Gamma E_{1o}^i}{\eta}\sin\theta_i^P e^{-j\beta_{1y}h/2}, \tag{29}$$

$$H_x|_{0,-\frac{1}{2}}^{n} \rightarrow \frac{E_{1o}^i}{\eta}\sin\theta_i^P e^{j\beta_{1y}h/2} + \frac{\Gamma E_{1o}^i}{\eta}\sin\theta_i^P e^{j\beta_{1y}h/2} \tag{30}$$

where η is the dispersion-immune intrinsic wave impedance [9]. Assembling these substitutions into equation (25) and simplifying we get

$$\begin{aligned}\frac{j2h(1+\Gamma)}{c\Delta t}\sin(\omega\Delta t/2) \;=\;& -(1+\Gamma)\cos\theta_t^P e^{-j\beta_{2x}h/2} \\ &+ \cos\theta_i^P\left(e^{j\beta_{1x}h/2} - \Gamma e^{-j\beta_{1x}h/2}\right) \\ &+ j2(1+\Gamma)\sin\theta_i^P\sin(\beta_{1y}h/2).\end{aligned} \tag{31}$$

Splitting the reflection coefficient into its real and imaginary parts ($\Gamma = \Gamma_r + j\Gamma_i$) and decoupling the complex equation we can write,

$$\left[\begin{array}{c} -(1+\Gamma_r)\cos\theta_t^P\cos\frac{\beta_{2x}h}{2} \\ +(1-\Gamma_r)\cos\theta_i^P\cos\frac{\beta_{1x}h}{2}\end{array}\right] = \Gamma_i\left[\begin{array}{c} -\frac{2h}{c\Delta t}\sin\frac{\omega\Delta t}{2} + \cos\theta_t^P\sin\frac{\beta_{2x}h}{2} \\ +\cos\theta_i^P\left(\cos\frac{\beta_{1x}h}{2} + \sin\frac{\beta_{1x}h}{2}\right)\end{array}\right] \tag{32}$$

and

$$\Gamma_i\left[\cos\theta_t^P\sin\frac{\beta_{2x}h}{2} + \cos\theta_i^P\cos\frac{\beta_{1x}h}{2}\right] = \tag{33}$$
$$(1+\Gamma_r)\left[\begin{array}{c} -\frac{2h}{c\Delta t}\sin\frac{\omega\Delta t}{2} + 2\sin\theta_i^P\sin\frac{\beta_{1y}h}{2} \\ +\cos\theta_t^P\sin\frac{\beta_{2x}h}{2} + \cos\theta_i^P\sin\frac{\beta_{1x}h}{2}\end{array}\right].$$

Equations (32) and (33) are satisfied by a real-valued Γ which reduces (32) (when $\Gamma_i = 0$) to

$$(1-\Gamma_r)\cos\theta_i^P\cos\frac{\beta_{1x}h}{2} - (1+\Gamma_r)\cos\theta_t^P\cos\frac{\beta_{2x}h}{2} = 0 \tag{34}$$

from which the closed-form expression of the numerical reflection coefficient can be written as,

$$\Gamma = \frac{1-\kappa}{1+\kappa} \qquad \text{with} \qquad \kappa = \frac{\cos\theta_t^P\cos\frac{\beta_{2x}h}{2}}{\cos\theta_i^P\cos\frac{\beta_{1x}h}{2}}. \tag{35}$$

For any incidence angle θ_i, β_{1x} and β_{1y} are obtained from the left zonal dispersion relation. β_{2x} is then calculated from the right zonal dispersion relation after setting $\beta_{2y} = \beta_{1y}$, which would also yield θ_t. This is followed by finding θ_i^P and θ_t^P using equation (23), then finally Γ is calculated from equation (35).

IV. S_{24}/S_{22} HYBRID ALGORITHM IN 2-D

Starting with the hybrid S_{24}/S_{22} algorithm let us first observe the deviations of the polarization angle from the propagation angle, $\theta^P - \theta$, as a function of the incidence angle θ_i in both zones (Fig. 3). As shown, grid symmetry aligns both angles when the incidence angle is either zero or $\pi/4$. At other angles, however, the deviation in the S_{22} zone reaches as high as 25 times that in the S_{24} zone at the uniform resolution of $R = 10$ cells per wavelength. Furthermore, as $\theta_i \rightarrow \pi/2$ the boundary condition (24) forces an exaggerated error in both transmission angles, θ_t and θ_t^P as shown in Figs. 3 and 4. Figure 5 compares the numerical reflection coefficient at different resolution factors versus angle of incidence (solid lines). It is clear from the figure that spurious reflections can become problematic as the incidence angle goes beyond 80° unless fine meshing is used which negates the computational efficiency advantage of the high-order S_{24} algorithm.

To solve this problem of increasing reflections near grazing angles, the S_{22} algorithm in the right zone is modified so that second order differencing is maintained for $\partial/\partial x$ and a fourth order differencing is applied to $\partial/\partial y$ as demonstrated in Fig. 6. This approach

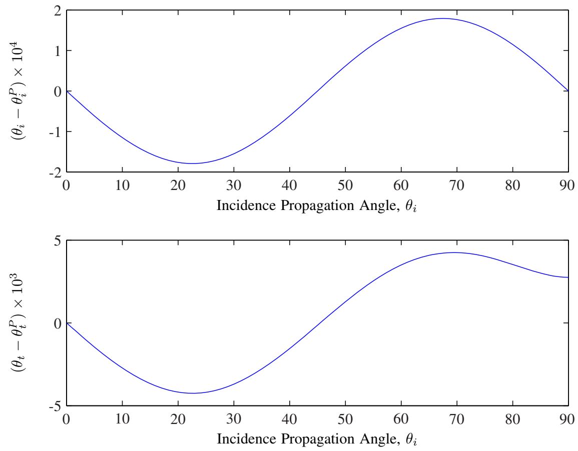

Fig. 3. Deviation between propagation and polarization angles in both incidence and transmission zones. $R = 10$ cells per wavelength.

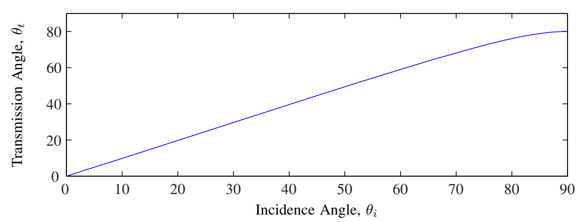

Fig. 4. Effect of boundary conditions at the $x = 0$ interface on the transmission angle. $R = 10$ cells per wavelength.

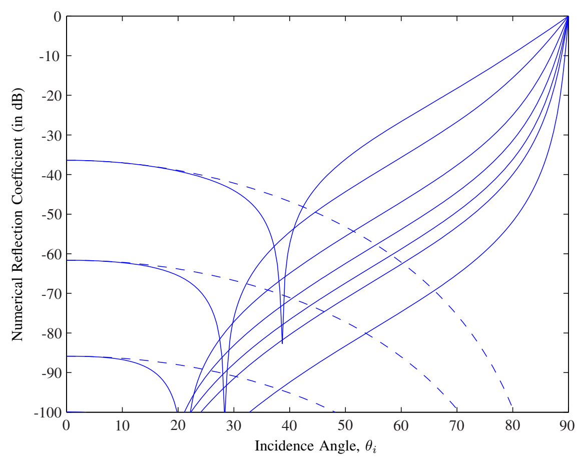

Fig. 5. Numerical reflection coefficient vs. θ_i across an S_{24}/S_{22} hybrid algorithm interface before (solid) and after (dashed) tangential phase matching at the resolution factors (from top to bottom), $R = 5, 10, 20, 30, 40, 50, 100$.

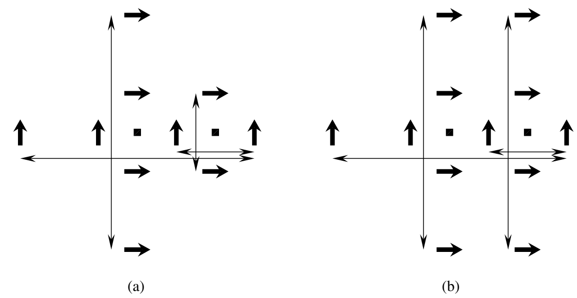

Fig. 6. FDTD stencil extents at the S_{24}/S_{22} interface before (a) and after (b) tangential stretching in the S_{22} zone for phase matching purposes.

has the advantage of single-cell interface-normal depth for modeling physical discontinuities and an extended interface-tangential cell that matches the numerical wavenumbers along that direction. The corresponding update equations for the $y-$stretched algorithm in zone 2 are given by,

$$\begin{aligned}
\epsilon \frac{\partial E_z}{\partial t} &= \frac{H_y|_{i+\frac{1}{2}} - H_y|_{i-\frac{1}{2}}}{h} \\
&\quad - \frac{27(H_x|_{j+\frac{1}{2}} - H_x|_{j-\frac{1}{2}})}{24h} \\
&\quad + \frac{H_x|_{j+\frac{3}{2}} - H_x|_{j-\frac{3}{2}}}{24h} \\
\mu \frac{\partial H_y}{\partial t} &= \frac{E_z|_{i+\frac{1}{2}} - E_z|_{i-\frac{1}{2}}}{h} \\
\mu \frac{\partial H_x}{\partial t} &= -\frac{27(E_z|_{j+\frac{1}{2}} - E_z|_{j-\frac{1}{2}})}{24h} \\
&\quad + \frac{E_z|_{j+\frac{3}{2}} - E_z|_{j-\frac{3}{2}}}{24h}
\end{aligned} \tag{36}$$

and the discrete operators which would replace those of equation (3) are

$$D_x = \frac{\sin\frac{\beta_x h}{2}}{h/2}, \tag{37}$$

$$D_y = \frac{9}{8}\frac{\sin\frac{\beta_y h}{2}}{h/2} - \frac{1}{8}\frac{\sin\frac{3\beta_y h}{2}}{3h/2}. \tag{38}$$

The corresponding dispersion relation is obtainable from equation (16) and the stability limit is governed by,

$$\Delta t \leq \frac{h}{c\sqrt{2}}\sqrt{\frac{72}{85}} \tag{39}$$

a slightly more relaxed condition than that of the left zone's S_{24} algorithm ensuring stability when the latter is enforced. Figure 5 (dashed lines) demonstrates the advantage gained in the form of vanishing reflections at near-grazing incidence angles.

It must be remembered that the numerical reflection coefficient (35) was derived using the S_{22} update equation (25) at the interface. The corresponding expression

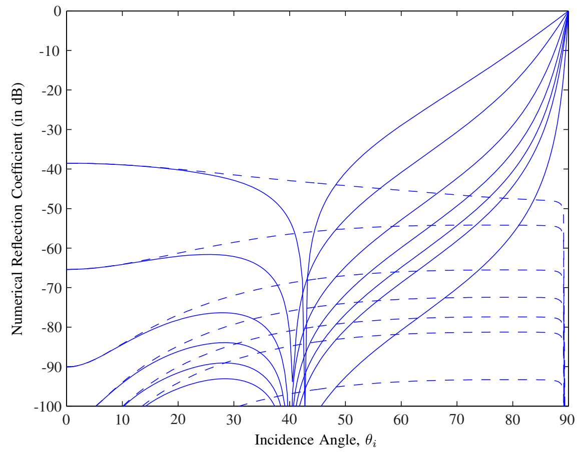

Fig. 7. Numerical reflection coefficient vs. θ_i across an M24/S$_{22}$ hybrid algorithm interface before (solid) and after (dashed) tangential phase matching at the resolution factors (from top to bottom) $R = 5, 10, 20, 30, 40, 50, 100$.

for the above phase-matched S$_{24}$/S$_{22}$ interface must be derived from,

$$E_z|_{0,0}^{n+\frac{1}{2}} = E_z|_{0,0}^{n-\frac{1}{2}} + \frac{\Delta t}{\epsilon h}\left(H_y|^n_{\frac{1}{2},0} - H_y|^n_{-\frac{1}{2},0}\right) - \frac{\Delta t}{24\epsilon h}\begin{pmatrix} 27H_x|^n_{0,\frac{1}{2}} - 27H_x|^n_{0,-\frac{1}{2}} \\ -H_x|^n_{0,\frac{3}{2}} + H_x|^n_{0,-\frac{3}{2}} \end{pmatrix} \tag{40}$$

which necessitates an additional substitution to equations (26) to (30);

$$H_x|^n_{0,\pm\frac{3}{2}} \rightarrow \frac{(1+\Gamma)E^i_{1o}}{\eta}\sin\theta^P_i e^{\mp j3\beta_{1y}h/2}. \tag{41}$$

Completing the substitutions into equation (40) will only affect the term containing β_{1y} in (31), leaving (32) and the Γ_i term in (33) intact and in a manner that maintains equation's (35) validity for predicting the numerical reflection coefficient across the interface in the present case.

V. M24/S$_{22}$ HYBRID ALGORITHM

As in the case of the S$_{24}$/S$_{22}$ interface, variations in the M24 algorithm's dispersion behavior versus propagation angle compared to those of the S$_{22}$ algorithm cause serious spurious numerical reflections at near grazing angles at the interface as demonstrated in Fig. 7 (solid lines). To remedy these high reflections the S$_{22}$ algorithm in the right zone needs to be replaced by one that maintains single cell normal depth but has matching tangential dispersion characteristics to the left zone M24 algorithm. A logical choice would be to apply the M24 development methodology using concentric flat (one cell depth along the x-axis) Ampere's and Faraday's loops. However, such an approach would be an overkill and is unnecessary, considering that in real applications the right zone would be only one cell deep negating the need for low dispersion for all propagation angles save for the tangential direction to the interface. A simpler and more practical scheme is to use again an elongated S$_{22}$ algorithm as in the previous case, except that a tuning parameter is introduced to be used for phase matching with the left M24 zone,

$$\begin{aligned}
\epsilon\frac{\partial E_z}{\partial t} &= \frac{H_y|_{i+\frac{1}{2}} - H_y|_{i-\frac{1}{2}}}{h} \\
&\quad + \frac{K^b}{3h}(H_x|_{j-\frac{3}{2}} - H_x|_{j+\frac{3}{2}}) \\
&\quad + \frac{1-K^b}{h}(H_x|_{j-\frac{1}{2}} - H_x|_{j+\frac{1}{2}}) \\
\mu\frac{\partial H_y}{\partial t} &= \frac{E_z|_{i+\frac{1}{2}} - E_z|_{i-\frac{1}{2}}}{h} \\
\mu\frac{\partial H_x}{\partial t} &= \frac{K^b}{3h}(E_z|_{j-\frac{3}{2}} - E_z|_{j+\frac{3}{2}}) \\
&\quad + \frac{1-K^b}{h}(E_z|_{j-\frac{1}{2}} - E_z|_{j+\frac{1}{2}}).
\end{aligned} \tag{42}$$

The corresponding discrete operators are

$$D_x = \frac{\sin\frac{\beta_x h}{2}}{h/2}, \tag{43}$$

$$D_y = (1-K^b)\frac{\sin\frac{\beta_y h}{2}}{h/2} + K^b\frac{\sin\frac{3\beta_y h}{2}}{3h/2}, \tag{44}$$

with the dispersion relation obtainable from equation (16) and the stability limit governed by

$$\Delta t \leq \frac{h}{c}\frac{1}{\sqrt{1+(1-4K^b/3)^2}}. \tag{45}$$

The choice for the tuning parameter K^b will be based on an optimization routine that will minimize the numerical reflection coefficient (equation (35) is valid for this case too) for the particular resolution factor R used in the simulation. Table 1 lists the K_1 and K_2 parameters for the left zone at several R values along with matching K^b values for the right zone that will eliminate spurious reflections at the interface as shown in Fig. 7 (dashed lines).

VI. NUMERICAL VALIDATION

To verify the effectiveness of the modified update equations (36) and (42) at eliminating reflections off the S$_{24}$/S$_{22}$ and M24/S$_{22}$ interfaces, FDTD simulations were performed where a point sinusoidal source was initiated very near the interfaces (4 cells away) to highlight near-grazing wave incidence. The simulations were run once with high-order update equations for the left zone and S$_{22}$ update equations for the right zone, and again with the former applied to both zones. Figure 8 highlights the absolute difference between the

Table 1. K_1 and K_2 values for the left zone M24 algorithm with corresponding K^b values for a phase-matched right zone S_{22} algorithm.

R	K_1	K_2	K^b
5	-0.144932	0.1020689	-0.0933211
10	-0.116193	0.0734445	-0.0793836
20	-0.110322	0.0678920	-0.0763555
30	-0.109283	0.0669205	-0.0758122
40	-0.108922	0.0665844	-0.0756233
50	-0.108756	0.0664296	-0.0755362
100	-0.108535	0.0662238	-0.0754201

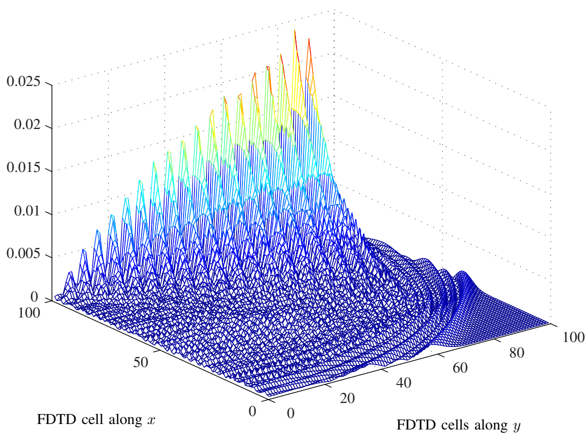

Fig. 8. Isolated numerical reflections at the interface of a typical hybrid S_{24}/S_{22} algorithm. $R = 10$ at 1 GHz.

two simulation runs for the S_{24}/S_{22} case isolating net numerical reflections off the interface.[1] Note in this figure the increasing reflection noise levels as the surface wave propagates further away from the source location along the interface. In comparison, Fig. 9 demonstrates the total absence of this interface hugging reflection noise due to the implementation of equations (36) in the right zone. Figures 10 and 11 demonstrate a similar accomplishment for the M24/S_{22} case. Table 2 summarizes a comparison between these measured after-modification reflections and those predicted in Figs. 5 and 7 showing reasonable agreements, especially in the M24/S_{22} case.

Finally, reflection noise levels could be further reduced by using a soft-start sinusoidal source. For example, using Furse *et al.*'s raised cosine ramp function [11],

$$r(t) = \begin{cases} 0, & t < 0 \\ \frac{1}{2}\left(1 - \cos\frac{\omega t}{2\alpha}\right), & 0 \le t \le \alpha T \\ 1, & t > \alpha T \end{cases} \quad (46)$$

[1]Only the upper-left quadrant data of Fig. 2 are shown as the reflections were symmetric across the x-axis.

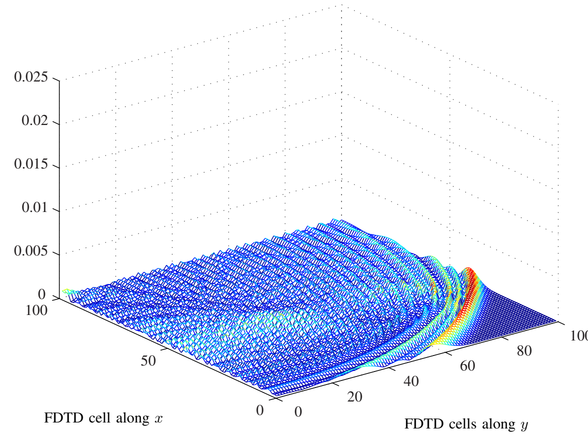

Fig. 9. Elimination of tangential reflections due to S_{22} phase-matching with the S_{24} scheme in a hybrid S_{24}/S_{22} algorithm. $R = 10$ at 1 GHz.

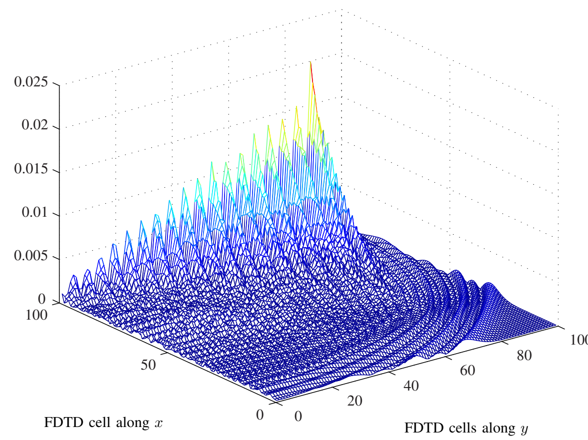

Fig. 10. Isolated numerical reflections at the interface of a typical hybrid M24/S_{22} algorithm. $R = 10$ at 1 GHz.

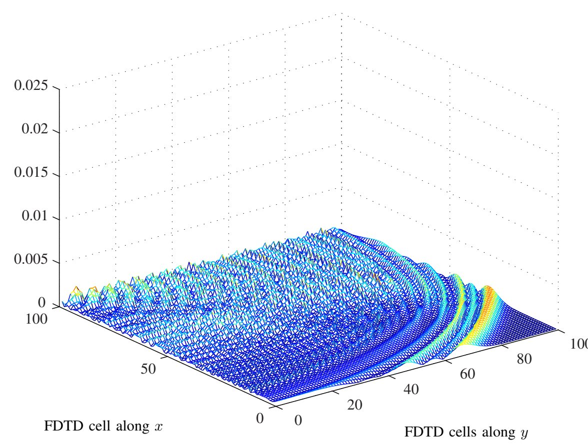

Fig. 11. Elimination of tangential reflections due to S_{22} phase-matching with the M24 scheme in a hybrid M24/S_{22} algorithm. $R = 10$ at 1 GHz.

Table 2. Comparison of predicted and measured numerical reflections after phase-matching the high-order and low-order schemes in the hybrid algorithms discussed in this work. $R = 10$ at 1 GHz.

Algorithm	Predicted $\Gamma_{\max}$	Measured $\Gamma_{\max}$
S_{24}/S_{22}	-62 dB	-55 dB
$M24/S_{22}$	-54 dB	-57 dB

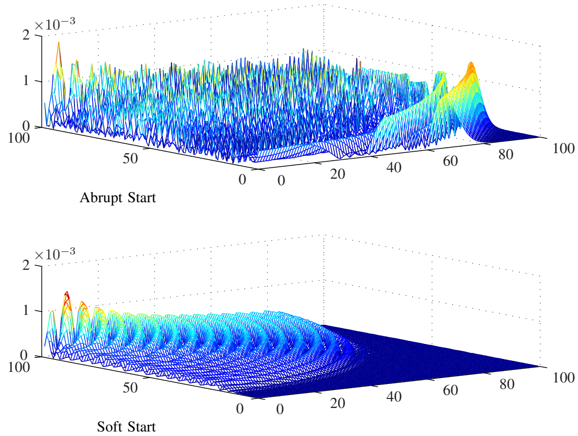

Fig. 12. Filtering out high-frequency content of the reflection noise in the phase-matched hybrid $M24/S_{22}$ algorithm by replacing the abruptly-starting sine source with a smooth-starting ramped-cosine source.

with $T = 2\pi/\omega$ and α chosen as 1.5, we can replace the $\sin(\omega t)$ source in the FDTD simulations with $r(t)\cos(\omega t)$. Such a substitution would effectively filter out the high frequency content of the reflection noise as demonstrated in Fig 12.

VII. CONCLUSION

The phase velocity mismatches across hybrid high-order/low-order FDTD implementations cause unacceptably growing reflections across the hybrid interface when the traversing wave is at near grazing incidence angles. A predictive equation of the ensuing numerical reflections has been derived, investigated and used along with the dispersion relations of both the high-order and low-order schemes to modify the latter and match its tangential (to the interface) phase velocity to that of the former. Numerical experiments have demonstrated that this modification has completely eliminated the excessive interface-hugging reflection noises and reduced them to the same level as the axial reflection noises. These experiments have been performed for the S_{24}/S_{22} and $M24/S_{22}$ hybrid algorithms with good agreement between predicted and measured reflections after the phase-matching algorithm modifications. In practical applications this innovation allows efficient use of thin (one cell deep) S_{22} buffer zones where needed in an otherwise global high-order implementation for modeling electrically large structures with high phase accuracy.

REFERENCES

[1] K. L. Shlager and J. B. Schneider, "Comparison of the dispersion properties of several low-dispersion finite-difference time-domain algorithms," *IEEE Trans. Antennas Propagat.*, vol. 51, no. 3, pp. 642–653, Mar. 2003.

[2] E. A. Forgy and W. C. Chew, "A time-domain method with isotropic dispersion and increased stability on an overlapped lattice," *IEEE Trans. Antennas Propagat.*, vol. 50, no. 7, pp. 983–996, July 2002.

[3] J. B. Cole, "A high-accuracy realization of the Yee algorithm using non-standard finite differences," *IEEE Trans. Microwave Theory Tech.*, vol. 45, no. 6, pp. 991–996, June 1997.

[4] M. F. Hadi and M. Piket-May, "A modified FDTD (2,4) scheme for modeling electrically large structures with high-phase accuracy," *IEEE Trans. Antennas Propagat.*, vol. 45, no. 2, pp. 254–264, Feb. 1997.

[5] G. J. Haussmann, "A dispersion optimized three-dimensional finite-difference time-domain method for electromagnetic analysis," Ph.D. dissertation, University of Colorado at Boulder, Boulder, CO, 1998.

[6] S. V. Georgakopoulos, R. A. Renaut, C. A. Balanis, and C. R. Birtcher, "A hybrid fourth-order FDTD utilizing a second-order FDTD subgrid," *IEEE Microwave Wireless Compon. Lett.*, vol. 11, no. 11, pp. 462–464, Nov. 2001.

[7] M. Celuch-Marcysiak, "Extended study of poynting theorem and reciprocity on nonuniform fdtd meshes," *IEE Proc.-Sci. Meas. Technol.*, vol. 151, no. 6, pp. 452–455, Nov. 2004.

[8] M. Celuch-Marcysiak and J. Rudnicki, "A study of numerical reflections caused by fdtd mesh refinements in 1d and 2d," *15th Ann. Conf. Microwave Radar Wireless Comm., Warsaw, Poland*, pp. 626–629, May 2004.

[9] M. Celuch-Marcysiak and W. K. Gwarek, "On the nature of solutions produced by finite difference schemes in time domain," *Int. J. Numerical Modelling: Electronic Networks, Devices and Fields*, vol. 12, no. 1–2, pp. 23–40, Jan.–Apr. 1999.

[10] J. B. Schneider, "Plane waves in FDTD simulations and a nearly perfect total-field/scattered-field boundary," *IEEE Trans. Antennas Propagat.*, vol. 52, no. 12, pp. 3280–3287, Dec. 2004.

[11] C. M. Furse, D. H. Roper, D. N. Buechler, D. A. Christensen, and C. H. Durney, "The problem and treatment of DC offsets in FDTD simulations," *IEEE Trans. Antennas Propagat.*, vol. 48, no. 58, pp. 1198–1201, Aug. 2000.

Mohammed Hadi was born in 1965. He received his B.S. degree in electrical engineering from Kuwait University in 1988 and his M.S. and Ph.D. degrees from the University of Colorado at Boulder in 1992 and 1996. From his position as an Assistant Professor at the Department of Electrical Engineering of Kuwait University, Dr. Hadi kept himself busy for the last decade in governmental work and consultations in the areas of engineering training, higher education planning and Kuwait's labour profile studies. Dr. Hadi is currently a Visiting Research Scholar at Duke University, North Carolina.

Rabie Dib was born in 1977. He received his B.S. and M.S. degrees in electrical engineering from Kuwait University in 1999 and 2002. Mr. Dib worked as a Teaching Assistant and operated the Electromagnetic Compatibility Lab. at Kuwait University from 2000 to 2006 during which he participated in several intra-industry training programs. Mr. Dib is currently an Instructor with the College of Technological Studies at Kuwait's Public Authority of Applied Education and Training.